

CRAUM-Net: Contextual Recursive Attention with Uncertainty Modeling for Salient Object Detection

Abhinav Sagar

University of Maryland, College Park, Maryland
College Park, Maryland

asagar@umd.edu

Abstract

Salient Object Detection (SOD) plays a crucial role in many computer vision applications, requiring accurate localization and precise boundary delineation of salient regions. In this work, we present a novel framework that integrates multi-scale context aggregation, advanced attention mechanisms, and uncertainty-aware module for improved SOD performance. Our Adaptive Cross-Scale Context Module effectively fuses features from multiple levels, leveraging Recursive Channel Spatial Attention and Convolutional Block Attention to enhance salient feature representation. We further introduce an edge-aware decoder that incorporates a dedicated Edge Extractor for boundary refinement, complemented by Monte Carlo Dropout to estimate uncertainty in predictions. To train our network robustly, we employ a combination of boundary-sensitive and topology-preserving loss functions, including Boundary IoU, Focal Tversky, and Topological Saliency losses. Evaluation metrics such as uncertainty-calibrated error and Boundary F1 score, along with the standard SOD metrics, demonstrate our method's superior ability to produce accurate and reliable saliency maps. Extensive experiments validate the effectiveness of our approach in capturing fine-grained details while quantifying prediction confidence, advancing the state-of-the-art in salient object detection.

1. Introduction

Salient Object Detection (SOD) focuses on accurately identifying and segmenting the most visually distinctive objects within images. It plays a fundamental role in a wide range of computer vision applications such as image retrieval, object recognition, video analysis, and autonomous systems. Recent advances driven by deep convolutional neural networks have significantly improved the accuracy of saliency prediction. Despite significant progress driven by deep learning, challenges remain in effectively capturing multi-

scale context, preserving boundary details, and accurately modeling uncertainty.

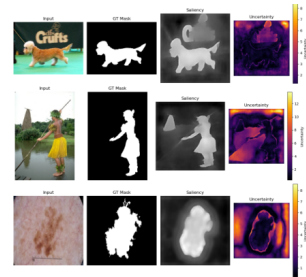


Figure 1. The three rows are samples from the datasets DUTS, ECSSD, and ISIC 2018, respectively. From left to right: input image, ground truth, saliency map, and uncertainty map from our method.

Uncertainty in SOD arises from multiple sources. Epistemic uncertainty reflects the model's lack of knowledge and can be reduced with more training data or improved architectures. Aleatoric uncertainty arises from noise and inherent ambiguity in the input data, such as occlusions, complex backgrounds, or low-quality images. Quantifying these uncertainties is crucial for deploying SOD models in real-world, safety-critical scenarios, where understanding the trustworthiness of predictions can prevent costly errors.

The four main contributions of our paper are as follows:

- We propose an Adaptive Cross-Scale Context Module that effectively integrates multi-scale features from previous, current, and lateral layers, combined with advanced attention mechanisms including Recursive Channel Spatial Attention and Convolutional Block Attention to enhance salient feature representation and context modeling.
- We design a hierarchical decoder incorporating boundary refinement via an Edge Extractor module and utilize Monte Carlo Dropout for uncertainty estimation, enabling both precise boundary recovery and reliable uncertainty quantification in saliency maps as shown in Figure 1.

- Our training framework employs novel loss functions, including boundary-aware and topology-preserving losses, along with novel evaluation metrics, including uncertainty-calibrated error and Boundary F1 score metrics, to ensure robust, accurate, and uncertainty-aware salient object detection.
- We conduct extensive experiments on standard SOD datasets to validate the effectiveness of our approach and demonstrate that our approach performs better than the state-of-the-art methods, while being interpretable at the same time.

2. Related Work

Salient Object Detection (SOD) has been extensively studied in computer vision to detect the most visually prominent objects in an image. Traditional methods relied on low-level cues such as color contrast, texture, and spatial heuristics [2, 23]. However, these handcrafted approaches were limited in handling complex scenes and diverse object appearances.

With the advent of deep learning, CNN-based methods have become the state of the art, exploiting hierarchical feature representations to capture semantic and structural information [24, 29, 46]. Multi-scale feature fusion [16, 43], attention mechanisms [41], and boundary refinement modules [46, 52] further improved detection accuracy and localization precision.

Methods like Amulet [51] introduced multi-level feature fusion and deep supervision, while architectures such as DSS [16] showed the importance of encoder-decoder structures for dense prediction. Recent works [24] emphasize the importance of boundary precision. By incorporating edge features or boundary-aware losses, these methods produce sharper object contours and improve segmentation accuracy around object borders.

[31] introduced U2-Net, a nested U-structure that effectively captures rich multi-scale features to enhance salient object detection with both accuracy and efficiency. Building on the concept of multi-scale contextual modeling, [22] proposed the Adjacent Context Coordination Network (ACCoNet), which facilitates cross-scale feature interaction specifically designed for salient object detection in optical remote sensing images. Complementing these approaches, [56] presented ADMNet, a lightweight and attention-guided densely multi-scale network that balances real-time performance with strong detection capabilities.

In the context of SOD, uncertainty modeling remains underexplored compared to other vision tasks. Some initial efforts have introduced confidence maps to detect uncertain or ambiguous regions [11, 36], while others have combined uncertainty estimation with multi-task learning [20], jointly predicting saliency and boundary uncertainty to improve segmentation quality. However, these approaches often fo-

cus on aleatoric uncertainty or employ heuristic confidence measures without principled Bayesian modeling. Moreover, a comprehensive evaluation of uncertainty measures and their practical benefits in SOD is still lacking.

Our approach addresses these gaps by proposing a unified Bayesian framework that explicitly models both epistemic and aleatoric uncertainty in salient object detection. We demonstrate through extensive experiments that uncertainty-aware saliency maps enable more reliable and interpretable predictions, particularly in challenging scenarios involving occlusion, clutter, and low contrast.

3. Methodology

3.1. Problem Definition

Given an input image $\mathbf{I} \in R^{H \times W \times 3}$, the goal of Salient Object Detection (SOD) is to predict a binary saliency map $\mathbf{S} \in \{0, 1\}^{H \times W}$ that highlights the most visually prominent objects in the scene. Formally, the task is to learn a mapping function

$$f : \mathbf{I} \rightarrow \hat{\mathbf{S}},$$

where $\hat{\mathbf{S}} \in [0, 1]^{H \times W}$ is a probabilistic saliency map representing the likelihood of each pixel belonging to a salient object.

3.2. Model Architecture

3.2.1. Backbone Feature Extraction

We adopt a modified ResNet50 backbone, denoted as Backbone.ResNet50.in3, which extracts feature maps $\{f_1, f_2, f_3, f_4, f_5\}$ at progressively deeper levels. Each feature map f_i is extracted at a spatial resolution of $\frac{1}{2^i}$ of the input image, with increasing channel depth, which are crucial for capturing both global context and fine-grained details necessary for accurate salient object detection.

3.2.2. Efficient Channel Attention (ECA) and Spatial Attention (SA) Mechanisms.

We implement an attention module inspired by the CBAM [44] framework, combining both channel and spatial attention to enhance feature representations. We replace the channel attention by the CBAM [44] with Efficient Channel Attention (ECA) [39]. The details of ECA, SA, and CBAM can be found in the Appendix.

3.2.3. Recursive Channel-Spatial Attention (RCSA).

To enhance feature representation by iteratively refining both channel and spatial dependencies, we introduce the *Recursive Channel-Spatial Attention (RCSA)* module. The architecture is defined as a recursive attention mechanism that performs joint channel and spatial attention updates over multiple steps, enabling deeper refinement of informative features and suppression of irrelevant activations.

Formally, let $x \in R^{C \times H \times W}$ be the input feature map, where C is the number of channels and $H \times W$ denotes the spatial resolution. The module initializes an attention state as $a_0 = x$ and refines it over T steps using both channel and spatial attention cues. Each step involves the following operations:

1. **Depthwise Projection:** A depthwise 1×1 convolution is applied to retain per-channel semantics while reducing parameter cost:

$$a'_t = \text{Conv}_{\text{depth}}(a_{t-1}) \quad (1)$$

2. **Channel Attention:** We extract channel-wise descriptors using global average pooling and apply a two-layer MLP with reduction ratio r followed by a sigmoid activation:

$$\mathbf{c}_t = \sigma(W_2 \cdot \text{ReLU}(W_1 \cdot \text{GAP}(a'_t))) \quad (2)$$

where σ denotes the sigmoid function, and W_1, W_2 are 1×1 convolutional weights with sizes $C \rightarrow C/r$ and $C/r \rightarrow C$, respectively.

The attention is then applied to modulate the features:

$$a_t^c = a'_t \cdot \mathbf{c}_t \quad (3)$$

3. **Spatial Attention:** We compute spatial descriptors by concatenating the channel-wise average and max projections:

$$s_t = \sigma(\text{Conv}_{7 \times 7}([\text{Avg}(a_t^c); \text{Max}(a_t^c)])) \quad (4)$$

where $[\cdot; \cdot]$ denotes channel-wise concatenation. This generates a spatial mask to refine salient regions.

4. **Recursive Update:** The attention state is updated by modulating the previous state with the spatial attention and adding the original residual:

$$a_t = a_{t-1} \cdot s_t + x \quad (5)$$

After T recursive steps, the final output is given by:

$$y = a_T + x \quad (6)$$

This residual connection ensures gradient flow and feature preservation.

3.2.4. Context Aggregation Module.

To effectively capture multi-scale contextual information, we design a *Context Aggregation Module* (CAM) that leverages parallel dilated convolutions with varying receptive fields. Given an input feature map $x \in R^{B \times C \times H \times W}$, the module applies three parallel 3×3 convolutional layers with increasing dilation rates $\{1, 3, 5\}$. These dilation rates enable the convolutions to sample from local, mid-range, and broader contexts without increasing the number of parameters or the computational burden significantly.

Formally, the output of each branch is computed as:

$$\begin{aligned} d_1 &= \text{ReLU}(\text{Conv}_{3 \times 3}^{\text{dilation}=1}(x)) \\ d_2 &= \text{ReLU}(\text{Conv}_{3 \times 3}^{\text{dilation}=3}(x)) \\ d_3 &= \text{ReLU}(\text{Conv}_{3 \times 3}^{\text{dilation}=5}(x)) \end{aligned}$$

The final output feature map is then obtained by element-wise summation of the three branches:

$$y = d_1 + d_2 + d_3$$

3.2.5. Edge Extractor Module.

To enhance boundary localization and guide structural learning, we introduce an *Edge Extractor Module* that explicitly captures edge information from input feature maps using Sobel operators. This module computes the image gradients along the horizontal and vertical directions using fixed convolutional filters and then refines the edge response via learnable convolutional layers.

Given an input feature map $x \in R^{B \times 1 \times H \times W}$, horizontal and vertical edges are extracted using classic Sobel kernels:

$$\text{Sobel}_x = \begin{bmatrix} -1 & 0 & 1 \\ -2 & 0 & 2 \\ -1 & 0 & 1 \end{bmatrix}, \quad \text{Sobel}_y = \begin{bmatrix} -1 & -2 & -1 \\ 0 & 0 & 0 \\ 1 & 2 & 1 \end{bmatrix}$$

These kernels are applied as fixed filters in a convolutional manner:

$$\text{edge}_x = \text{Conv2D}(x, \text{Sobel}_x), \quad \text{edge}_y = \text{Conv2D}(x, \text{Sobel}_y)$$

The gradient magnitude is then computed as:

$$\text{edges} = \sqrt{\text{edge}_x^2 + \text{edge}_y^2}$$

To adapt the raw edge maps to the downstream network, we apply a lightweight learnable refinement stage. This consists of a convolutional block (Conv-BN-ReLU) followed by a 1×1 convolution and a sigmoid activation:

$$\text{edges}_{\text{refined}} = \sigma(\text{Conv}_{1 \times 1}(\text{ConvBlock}(\text{edges})))$$

3.2.6. Adaptive Cross-Scale Context Module (ACSCM).

To effectively integrate multi-level features across different stages of the network, we design an Adaptive Cross-scale Context Module based on [22] that aggregates semantic information from three contexts: the *previous*, *current*, and *latter* stages. This module leverages multi-dilated convolutions and attention-based enhancement to form a spatially aware and contextually rich representation.

1. Multi-dilated Current Feature Extraction: To model the local and global context from the current stage feature map x_{cur} , we use four parallel dilated convolution blocks with dilation rates of 1, 2, 3, and 4:

$$x_{\text{cur}_i} = \text{Conv}_{d=i}(x_{\text{cur}}), \quad i \in \{1, 2, 3, 4\}$$

These outputs are concatenated and fused:

$$x_{\text{cur_all}} = \text{Conv}_{3 \times 3}(\text{Concat}[x_{\text{cur}_1}, x_{\text{cur}_2}, x_{\text{cur}_3}, x_{\text{cur}_4}])$$

2. Attention-based Refinement: To further enhance informative regions, the fused current features are passed through a channel-spatial attention module:

$$x_{\text{cur_att}} = \text{CBAM}(x_{\text{cur_all}})$$

3. Previous Feature Encoding: The previous feature map x_{pre} is downsampled to match the resolution of the current stage:

$$x_{\text{pre_down}} = \text{MaxPool2D}(x_{\text{pre}})$$

An attention mechanism is then applied:

$$x_{\text{pre_att}} = \text{CBAM}(x_{\text{pre_down}})$$

4. Latter Feature Encoding: The latter stage feature x_{lat} is upsampled and enhanced:

$$x_{\text{lat_up}} = \text{Upsample}(x_{\text{lat}}), \quad x_{\text{lat_att}} = \text{CBAM}(x_{\text{lat_up}})$$

5. Fusion of Multi-scale Context: All attended feature maps are adaptively aligned and added with a residual connection to the current input:

$$x_{\text{out}} = x_{\text{cur_att}} + x_{\text{pre_att}} + x_{\text{lat_att}} + x_{\text{cur}}$$

Variant - ACSCM1: We adopt a simplified variant, ACSCM1, which omits the latter branch and uses *Recursive Channel-Spatial Attention (RCSA)* instead of CBAM for both current and previous stages.

3.2.7. Decoder

To decode multi-level encoder features into a refined prediction map, we design a hierarchical decoder. This module exploits a sequence of dilated and standard convolutions to aggregate contextual information at multiple scales, followed by upsampling and fusion. Each block incorporates the following:

- A standard 3×3 convolution to reduce the input dimensionality.
- A dilated convolution (with dilation rates d_1 and d_2) to enlarge the receptive field without reducing resolution.
- Feature fusion using concatenation of intermediate features followed by a final 3×3 convolution.

Formally, for an input feature map $x \in R^{C_{in} \times H \times W}$, the block computes:

$$x_1 = \text{Conv}_{3 \times 3}(x), \quad (7)$$

$$x_1^d = \text{DilatedConv}_{d_1}(x_1), \quad (8)$$

$$x_2 = \text{Conv}_{3 \times 3}(x_1), \quad (9)$$

$$x_2^d = \text{DilatedConv}_{d_2}(x_2), \quad (10)$$

$$x_3 = \text{Conv}_{3 \times 3}(x_2), \quad (11)$$

$$y = \text{Conv}_{3 \times 3}([x_1^d, x_2^d, x_3]), \quad (12)$$

where $[\cdot]$ denotes channel-wise concatenation.

Progressive Decoding with Skip Fusion. We design a 5-stage decoder, each stage progressively refining features from coarse-to-fine by:

1. Merging upsampled decoder features with the corresponding encoder features via concatenation.
2. Applying the *Decoder* for local-global context refinement.
3. Upsampling the output to double its spatial resolution.
4. Producing intermediate supervision outputs at each stage via 3×3 convolution to encourage deep supervision.

Each decoder stage operates as follows:

$$x_i^{\text{up}} = \text{BAB_Decoder}([x_i, \text{Up}(x_{i+1}^{\text{up}})]), \quad (13)$$

$$s_i = \text{Conv}_{3 \times 3}(x_i^{\text{up}}), \quad (14)$$

where $i \in \{5, 4, 3, 2, 1\}$ indexes the decoder stages, and s_i is the output prediction at that stage. Bilinear upsampling is used throughout.

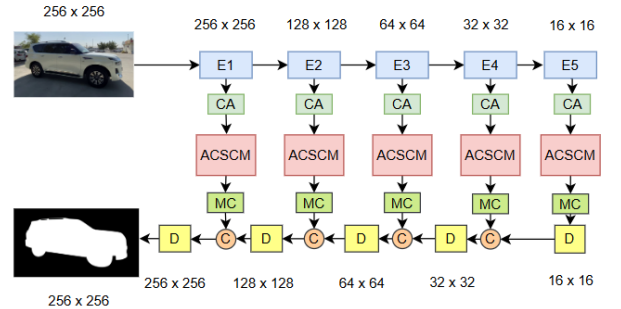


Figure 2. Illustration of the proposed network architecture diagram. Here E1, E2, E3, E4, and E5 denote the 5 encoders, CA denotes the Context Aggregation Module, ACSCM denotes the Adaptive Cross-Scale Context Module, MC denotes the Monte-Carlo dropout, D denotes the decoder, and C denotes the concatenation operation.

3.2.8. Uncertainty Quantification in Salient Object Detection

To effectively quantify uncertainty in our SOD framework, we employ Monte Carlo (MC) Dropout [13] as a practical Bayesian approximation. This approach allows us to estimate predictive uncertainty by performing multiple stochastic forward passes through the network at inference time, capturing model uncertainty caused by limited training data or model capacity.

Given an input image \mathbf{x} , the model outputs a saliency prediction $\hat{\mathbf{y}}$ by forwarding through the network with dropout enabled during inference. We perform T stochastic forward passes, obtaining a set of predictions $\{\hat{\mathbf{y}}^{(t)}\}_{t=1}^T$. The final saliency map $\hat{\mathbf{y}}$ is estimated as the expectation:

$$\hat{\mathbf{y}} = \frac{1}{T} \sum_{t=1}^T \hat{\mathbf{y}}^{(t)} \quad (15)$$

The predictive uncertainty is quantified by the variance of these predictions, reflecting the model’s confidence:

$$\mathbf{U} = \frac{1}{T} \sum_{t=1}^T \left(\hat{\mathbf{y}}^{(t)} - \hat{\mathbf{y}} \right)^2 \quad (16)$$

Here, \mathbf{U} is the pixel-wise uncertainty map, with higher values indicating regions where the model is less confident.

3.2.9. Final Prediction

The final prediction is generated by projecting the highest-resolution fused feature map to a single channel:

$$S = \sigma(\text{Conv}_{1 \times 1}(F_1)) \quad (17)$$

This output S represents the saliency map. Figure 2 illustrates the overall architecture of our proposed framework.

3.3. Loss Function

SOD demands not only accurate pixel-wise classification but also structural and topological fidelity. Traditional loss functions like Binary Cross-Entropy (BCE) may result in blurry or boundary-inaccurate predictions. To overcome these limitations, we propose a composite loss function that jointly optimizes pixel-level accuracy, overlap quality, boundary precision, and topological consistency.

1. Binary Cross-Entropy (BCE) Loss: The BCE loss is referred as \mathcal{L}_{BCE} . The details can be found in the Appendix.

2. IoU Loss: The IoU loss is referred as \mathcal{L}_{IoU} . The details can be found in the Appendix.

3. Focal Tversky (FT) Loss: The FT loss is referred as \mathcal{L}_{FT} . The details can be found in the Appendix.

4. Boundary IoU (BIOU) Loss: To sharpen object contours and improve boundary localization, we introduce the Boundary IoU loss. Unlike pixel-level or region-level losses, BIOU operates on edge maps derived via gradient approximations:

$$\mathcal{L}_{\text{BIOU}} = 1 - \frac{\sum(E_P \cdot E_G)}{\sum E_P + \sum E_G - \sum(E_P \cdot E_G) + \epsilon} \quad (18)$$

where E_P and E_G denote the predicted and ground truth edge maps, respectively, computed using horizontal and vertical edge differences.

5. Topological Saliency (TS) Loss: Salient objects are often expected to be structurally coherent (e.g., contiguous, hole-free regions). To preserve topological consistency, we present a Laplacian-based loss that compares structural contours:

$$\mathcal{L}_{\text{TS}} = \|\nabla^2(P > 0.5) - \nabla^2(G > 0.5)\|_1 \quad (19)$$

where P is the predicted probability map and G is the ground-truth binary map, ∇^2 is the discrete Laplacian operator, and $(\cdot > 0.5)$ is the binarization threshold.

Our final loss function is defined as:

$$\mathcal{L}_{\text{total}} = \lambda_1 \mathcal{L}_{\text{BCE}} + \lambda_2 \mathcal{L}_{\text{IoU}} + \lambda_3 \mathcal{L}_{\text{FT}} + \lambda_4 \mathcal{L}_{\text{BIOU}} + \lambda_5 \mathcal{L}_{\text{TS}} \quad (20)$$

where λ_i are weights empirically set to balance the contribution of each component. In our experiments, we empirically set the weights as:

$$\lambda_1 = 1.0, \quad \lambda_2 = 1.0, \quad \lambda_3 = 0.8, \quad \lambda_4 = 0.5, \quad \lambda_5 = 0.3$$

4. Experiments

4.1. Dataset

The following datasets were used to test and compare the performance of our method:

DUTS, ECSSD, HKU-IS, SBU-Shadow, and ISIC2018. The details can be found in the Appendix.

4.2. Implementation Details

We implemented our SOD framework using the PyTorch deep learning library. All experiments were conducted on a workstation equipped with an Nvidia A100 GPU, an Intel Core i9 CPU, and 128 GB RAM, running Ubuntu 20.04 and Python 3.10. All input images and corresponding ground truth saliency maps were resized to 256×256 before feeding into the network. We used the Adam optimizer with an initial learning rate of 1×10^{-4} and weight decay of 5×10^{-4} . The learning rate was scheduled to decay using a polynomial annealing policy. Models were trained for 100 epochs with a batch size of 4. Gradient clipping was applied with a threshold of 1.0 to stabilize training. During testing, only resizing and normalization were applied. The final saliency maps were upsampled to the original image resolution using bilinear interpolation.

4.3. Evaluation Metrics

To comprehensively assess the performance of the SOD models, we employ a suite of widely adopted evaluation metrics. These metrics quantify different aspects of prediction quality, including pixel-level accuracy, structural consistency, and region-level overlap with ground truth annotations.

Mean Absolute Error (MAE), F-measure F_{\max} , F_{adaptive} , and F_{weighted} , Structure Measure (S_α), Enhanced-alignment Measure (E_ϕ), and Intersection over Union (IoU). The details can be found in the Appendix.

We propose 2 new evaluation metrics for SOD: Uncertainty-Calibrated Error and Boundary-aware F-measure, as explained below:

Uncertainty-Calibrated Error (UCE). Traditional saliency metrics such as MAE or F-measure evaluate the correctness of predictions but do not account for the model’s confidence in its outputs. The Uncertainty-Calibrated Error (UCE) bridges this gap by integrating the model’s predictive uncertainty into error evaluation. It penalizes predictions that are both wrong and overconfident, aligning with the principle that a well-calibrated model should be uncertain when it is likely to err. Formally, for a probabilistic prediction $\hat{Y} \in [0, 1]$ and a ground truth mask $Y \in \{0, 1\}$, UCE is defined as:

$$\text{UCE} = E \left[\left(1 - \mathcal{H}(\hat{Y}) \right) \cdot 1_{|\hat{Y} - Y| > \delta} \right], \quad (21)$$

where δ is a predefined error tolerance ($\delta = 0.5$), and $\mathcal{H}(\hat{Y})$ is the binary entropy of the prediction:

$$\mathcal{H}(\hat{Y}) = -\hat{Y} \log \hat{Y} - (1 - \hat{Y}) \log(1 - \hat{Y}). \quad (22)$$

The UCE term $(1 - \mathcal{H}(\hat{Y}))$ penalizes confident predictions (low entropy), while $1_{|\hat{Y} - Y| > \delta}$ ensures that only significantly incorrect predictions are considered.

Intuitively, UCE is high when the model makes wrong predictions with high confidence, and low when errors are accompanied by high uncertainty. UCE rewards uncertainty in ambiguous regions (e.g., edges, occlusions). High UCE would correlate with robustness failures in safety-critical or low-data regimes. In practice, UCE is especially relevant in SOD tasks involving ambiguous foreground-background transitions. Lower UCE values indicate better error-uncertainty alignment and improved trustworthiness in model predictions.

Boundary-aware F-measure (B-F1). While traditional F-measure evaluates saliency prediction at the pixel level, it does not explicitly consider the spatial quality of object boundaries. The Boundary-aware F-measure (B-F1) addresses this by evaluating how well the predicted and ground truth boundaries align. First, the boundary maps of both the predicted saliency mask P and the ground truth Y are extracted using morphological gradient operations (dilation minus erosion). A tolerance-based matching is then performed using a disk-shaped structuring element of

a given radius (2 pixels), allowing for slight misalignments between boundary pixels.

$$\text{BF1} = \frac{2 \cdot \text{Precision}_b \cdot \text{Recall}_b}{\text{Precision}_b + \text{Recall}_b}, \quad (23)$$

where

$$\begin{aligned} \text{Precision}_b &= \frac{|\text{PB} \cap \text{DGTB}|}{|\text{PB}|}, \\ \text{Recall}_b &= \frac{|\text{GTB} \cap \text{DPB}|}{|\text{GTB}|}. \end{aligned} \quad (24)$$

Here, PB denotes Predicted Boundary, DGTB denotes Dilated Ground Truth Boundary, GTB denotes Ground Truth Boundary, and DPB denotes Dilated Predicted Boundary, respectively. The dilation accounts for localization tolerance, ensuring that near-boundary matches are rewarded. A higher B-F1 indicates sharper, more accurate boundary predictions.

Computational Efficiency Metrics. Number of Parameters (Params) in Millions, Floating Point Operations (FLOPs), Inference Time in milliseconds (ms), and Frames Per Second (FPS). The details can be found in the Appendix. All computational metrics are measured under standardized conditions: batch size of 1, fixed input resolution (256×256), and on the same hardware.

4.4. Performance Comparisons

We compare our model with other state-of-the-art salient object detection methods. The performance of these methods is reproduced using open-sourced implementations provided by the respective authors, under similar experimental settings. All models are evaluated on the same testing datasets and with the same preprocessing and resolution configurations.

4.4.1. Quantitative Performance

We evaluate the models in terms of performance and computational complexity. Table 1 summarizes the quantitative results on multiple benchmark datasets, including DUTS-TE, ECSSD, HKU-IS, SBU-Shadow, and the ISIC 2018 dataset with other state-of-the-art methods.

Our proposed method outperforms existing models across multiple metrics and datasets, demonstrating its superior ability to detect salient objects.

4.4.2. Qualitative Performance

Figure 3, 4 and 5 show visual comparisons of our method against several baselines. Our model accurately delineates salient regions, preserves boundary structures, and avoids false positives in complex backgrounds.

Overall, these results confirm the effectiveness of incorporating uncertainty estimation into the SOD pipeline, improving both prediction quality and model trustworthiness.

Table 1. A: Quantitative comparison of our approach with other state-of-the-art methods on the following datasets: A: DUTS, B: ECSSD, C: HKU-IS, D: SBU-Shadow, E: ISIC 2018. The best values are highlighted in blue.

Method	A: DUTS Dataset												
	MAE ↓	$F(m) \uparrow$	$F(a) \uparrow$	$F(w) \uparrow$	$S \uparrow$	$E \uparrow$	IoU \uparrow	UCE \downarrow	B-F1 \uparrow	Params \downarrow	Flops \downarrow	Time \downarrow	FPS \uparrow
ACCoNet [22]	0.0544	0.8792	0.7705	0.7947	0.8570	0.9248	0.7209	0.2325	0.6460	127.01	51.33	0.0179	55.96
ADMNet [56]	0.0915	0.7794	0.6490	0.6803	0.7721	0.8719	0.5847	0.2515	0.4925	0.84	0.42	0.0293	34.16
BBRF [26]	0.0486	0.8462	0.7848	0.7824	0.8476	0.8714	0.7023	0.0751	0.6594	74.40	27.12	0.1200	8.33
C2FNet [34]	0.0619	0.8680	0.6909	0.7923	0.8459	0.9249	0.7119	0.2528	0.6124	28.41	6.96	0.0253	39.46
CorrNet [15]	0.0925	0.7877	0.7216	0.5358	0.6932	0.8335	0.4371	0.2005	0.4293	4.09	21.31	0.0094	106.91
MINet [32]	0.0951	0.7781	0.6282	0.6477	0.7593	0.8857	0.5583	0.2537	0.4397	0.28	0.16	0.2152	4.65
SOC [10]	0.0522	0.8946	0.7566	0.7616	0.8503	0.9491	0.6964	0.2872	0.5678	100.01	100.98	0.0107	93.45
U2Net [31]	0.0653	0.8343	0.7171	0.7549	0.8274	0.8961	0.6736	0.2168	0.6098	44.01	37.65	0.0395	25.34
Ours	0.0502	0.8597	0.7780	0.8042	0.8566	0.9041	0.7247	0.2036	0.6901	153.57	61.56	0.1030	9.71
B: ECSSD Dataset													
ACCoNet [22]	0.0409	0.9597	0.8838	0.9033	0.9142	0.9514	0.8556	0.2916	0.7307	127.01	51.33	0.0177	56.58
ADMNet [56]	0.0755	0.9100	0.8207	0.8182	0.8433	0.8911	0.7417	0.2985	0.5931	0.84	0.42	0.0293	34.16
BBRF [26]	0.0433	0.9351	0.8764	0.8899	0.8972	0.9170	0.8333	0.0615	0.7608	74.40	27.12	0.1436	6.96
C2FNet [34]	0.0453	0.9461	0.8187	0.8975	0.9034	0.9470	0.8429	0.2998	0.6999	28.41	6.96	0.0301	33.20
CorrNet [15]	0.1302	0.8720	0.8277	0.5968	0.6963	0.7827	0.5001	0.2671	0.4446	4.09	21.31	0.0093	107.02
MINet [32]	0.0845	0.9088	0.8006	0.7936	0.8343	0.8859	0.7238	0.3048	0.5351	0.28	0.16	0.1896	5.27
SOC [10]	0.0543	0.9579	0.8791	0.8608	0.8914	0.9473	0.8113	0.3390	0.6291	100.01	100.98	0.0084	119.00
U2Net [31]	0.0535	0.9411	0.8628	0.8739	0.8895	0.9228	0.8151	0.2535	0.7111	44.01	37.65	0.0419	23.89
Ours	0.0408	0.9495	0.8754	0.9041	0.9067	0.9395	0.8500	0.2693	0.7848	153.57	61.56	0.1055	9.48
C: HKU-IS Dataset													
ACCoNet [22]	0.0365	0.9481	0.8963	0.8831	0.9049	0.9540	0.8264	0.2463	0.7336	127.01	51.33	0.0214	46.70
ADMNet [56]	0.0673	0.8902	0.8014	0.7982	0.8371	0.9080	0.7147	0.2638	0.6014	0.84	0.42	0.0258	38.71
BBRF [26]	0.0391	0.9208	0.8898	0.8638	0.8826	0.9180	0.7952	0.0558	0.7440	74.40	27.12	0.1221	8.19
C2FNet [34]	0.0418	0.9359	0.8361	0.8788	0.8960	0.9518	0.8162	0.2561	0.6955	28.41	6.96	0.0242	41.33
CorrNet [15]	0.0955	0.8726	0.8366	0.6304	0.7268	0.8352	0.5267	0.2244	0.4993	4.09	21.31	0.0114	87.92
MINet [32]	0.0750	0.8883	0.7802	0.7698	0.8259	0.9054	0.6908	0.2695	0.5422	0.28	0.16	0.1964	5.09
SOC [10]	0.0443	0.9454	0.8774	0.8467	0.8897	0.9557	0.7931	0.3016	0.6476	100.01	100.98	0.0112	89.58
U2Net [31]	0.0451	0.9261	0.8580	0.8622	0.8876	0.9365	0.7995	0.2217	0.7144	44.01	37.65	0.0312	32.05
Ours	0.0334	0.9371	0.8969	0.8931	0.9041	0.9474	0.8334	0.2231	0.7802	153.57	61.56	0.1000	10.00
D: SBU-Shadow Dataset													
ACCoNet [22]	0.0360	0.9293	0.8051	0.8635	0.8713	0.9476	0.7947	0.2520	0.6899	127.01	51.33	0.0184	54.49
ADMNet [56]	0.1288	0.7594	0.6898	0.4798	0.6295	0.7581	0.3835	0.2996	0.3473	0.84	0.42	0.0246	40.60
BBRF [26]	0.0338	0.9216	0.8447	0.8682	0.8696	0.9256	0.7995	0.0502	0.7404	74.40	27.12	0.0754	13.27
C2FNet [34]	0.0387	0.9209	0.7978	0.8359	0.8593	0.9381	0.7672	0.2390	0.6372	28.41	6.96	0.0213	46.87
CorrNet [15]	0.0571	0.9127	0.8263	0.7808	0.8160	0.9294	0.6972	0.2429	0.5953	4.09	21.31	0.0111	90.42
MINet [32]	0.1497	0.7327	0.6427	0.3870	0.5836	0.7927	0.3136	0.2823	0.2518	0.28	0.16	0.1918	5.21
SOC [10]	0.0444	0.9347	0.8087	0.8183	0.8530	0.9527	0.7556	0.2771	0.5924	100.01	100.98	0.0119	84.21
U2Net [31]	0.0810	0.7955	0.6966	0.6927	0.7594	0.8167	0.6197	0.2322	0.5516	44.01	37.65	0.0642	15.58
Ours	0.0316	0.9303	0.8386	0.8736	0.8771	0.9457	0.8053	0.2238	0.7396	153.57	61.56	0.0991	10.09
E: ISIC Dataset													
ACCoNet [22]	0.0557	0.9265	0.7394	0.8815	0.8770	0.9142	0.8050	0.2891	0.4896	127.01	51.33	0.0182	54.84
ADMNet [56]	0.0639	0.9356	0.7735	0.8602	0.8684	0.8939	0.7844	0.2845	0.4815	0.84	0.42	0.0246	40.61
BBRF [26]	0.0575	0.9086	0.7602	0.8705	0.8727	0.8933	0.7931	0.0855	0.4888	74.40	27.12	0.0692	14.45
C2FNet [34]	0.0582	0.9196	0.7302	0.8791	0.8753	0.9159	0.8028	0.2931	0.4797	28.41	6.96	0.0208	48.01
CorrNet [15]	0.1406	0.8981	0.8387	0.6509	0.7320	0.7661	0.5655	0.2870	0.3975	4.09	21.31	0.0116	86.57
MINet [32]	0.0627	0.9583	0.7420	0.8631	0.8770	0.9186	0.7947	0.3027	0.4878	0.28	0.16	0.1856	5.39
SOC [10]	0.0601	0.9618	0.6893	0.8589	0.8827	0.9459	0.7947	0.3847	0.4264	100.01	100.98	0.0085	117.93
U2Net [31]	0.0623	0.9553	0.7522	0.8626	0.8734	0.9130	0.7879	0.1831	0.4685	44.01	37.65	0.0475	21.07
Ours	0.0550	0.9055	0.7349	0.8825	0.8752	0.9034	0.8075	0.2875	0.4981	153.57	61.56	0.1022	9.78

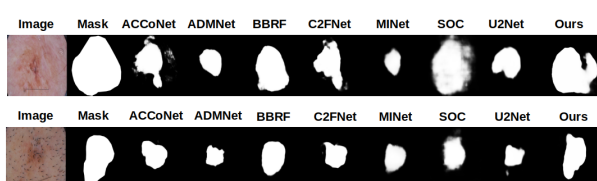


Figure 3. Qualitative comparison of different methods on the ISIC 2018 dataset. From left to right: input image, ground truth, ACCoNet, ADMNet, BBRF, C2FNet, MINet, SOC, U2Net, and our method.

4.5. Ablation Study

To rigorously evaluate the contribution of each proposed component in our uncertainty-aware salient object detection framework, we conduct comprehensive ablation studies using the DUTS dataset. We individually remove modules

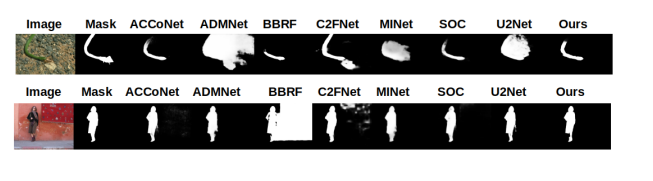


Figure 4. Qualitative comparison of different methods on the ECSSD dataset. From left to right: input image, ground truth, ACCoNet, ADMNet, BBRF, C2FNet, MINet, SOC, U2Net, and our method.

from the baseline to isolate and quantify their individual and joint effects.

Quantitative Results. Table 2 presents a comprehensive ablation study on the DUTS dataset to evaluate the impact of each component in our network architecture. We system-

Table 2. Ablation study on DUTS dataset by removing components. \downarrow : lower is better; \uparrow : higher is better. Best results in blue.

Method	MAE \downarrow	$F_m \uparrow$	$F_a \uparrow$	$F_w \uparrow$	$S \uparrow$	$E \uparrow$	IoU \uparrow	UCE \downarrow	B-F1 \uparrow	Param. \downarrow	FLOPs \downarrow	FPS \uparrow
W/o CA	0.0534	0.8584	0.7727	0.8054	0.8540	0.8973	0.7236	0.2052	0.6946	137.08	53.86	11.29
W/o CBAM	0.0506	0.8561	0.7753	0.8008	0.8558	0.8981	0.7211	0.1976	0.6868	153.54	61.54	10.44
W/o DropP.	0.0530	0.8580	0.7630	0.7949	0.8541	0.9034	0.7188	0.2490	0.6605	153.57	61.56	10.10
W/o Edge	0.0516	0.8570	0.7749	0.8060	0.8551	0.9014	0.7240	0.2016	0.6920	153.57	61.54	10.74
W/o MC Drop	0.0516	0.8582	0.7744	0.8028	0.8562	0.9001	0.7238	0.1989	0.6922	153.57	61.56	10.16
W/o RecAtt	0.0507	0.8565	0.7720	0.8009	0.8559	0.8910	0.7215	0.2007	0.6875	148.40	61.49	11.97
Ours	0.0502	0.8597	0.7780	0.8042	0.8566	0.9041	0.7247	0.2036	0.6901	153.57	61.56	9.71

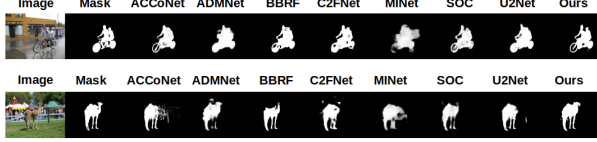


Figure 5. Qualitative comparison of different methods on the DUTS dataset. From left to right: input image, ground truth, ACCoNet, ADMNet, BBRF, C2FNet, MINet, SOC, U2Net, and our method.

Table 3. Ablation study on DUTS dataset by removing loss components. \downarrow lower is better; \uparrow higher is better. Best values are in blue.

Method	MAE \downarrow	$F_m \uparrow$	$F_a \uparrow$	$F_w \uparrow$	$S \uparrow$	$E \uparrow$	IoU \uparrow	UCE \downarrow	B-F1 \uparrow
W/o B-IOU	0.0484	0.8512	0.7769	0.8040	0.8606	0.9074	0.7163	0.2033	0.6792
W/o CE	0.0533	0.8206	0.7756	0.7973	0.8500	0.8506	0.7150	0.2087	0.6832
W/o FT	0.0537	0.8544	0.7701	0.7989	0.8535	0.9181	0.7206	0.2076	0.6846
W/o IOU	0.0495	0.8529	0.7754	0.7980	0.8556	0.9077	0.7189	0.2072	0.6804
W/o TS	0.0524	0.8518	0.7767	0.8003	0.8529	0.8820	0.7218	0.2003	0.6885
Ours	0.0502	0.8597	0.7780	0.8042	0.8566	0.9041	0.7247	0.2036	0.6901

atically remove one module at a time while keeping the rest of the architecture unchanged. The full model (denoted as "Ours") achieves the best overall performance in terms of F-measure variants, enhanced alignment (E), IoU, and overall structural quality, validating the synergy of all components.

Table 3 presents an ablation study assessing the impact of each individual loss function on the overall performance of our model. We systematically remove one loss term at a time from our full loss formulation and evaluate the model across several metrics. Overall, the full model—with all loss components combined—achieves the best balance across all performance metrics, thereby validating the complementary effects of our multi-term loss design.

Qualitative Analysis. Figure 6 visually illustrates the impact of removing individual architectural components on the saliency prediction quality, using samples from the DUTS dataset. Compared to the ground truth (B), the outputs from ablated models (C–I) exhibit various forms of degradation. In contrast, our full model (J) produces sharp, coherent, and spatially aligned saliency maps, affirming the synergistic contribution of each architectural component toward robust saliency detection.

Figure 7 presents a qualitative comparison of saliency



Figure 6. Qualitative ablation study by removing individual components from the network architecture using the DUTS dataset. A: Image, B: Ground Truth, C: Without CA Module, D: Without CBAM Attention, E: Without DropPath, F: Without Edge Extractor, G: Without MC Dropout, H: Without Recursive Attention, J: Our Model.

maps generated by ablated models trained without specific loss components, using the DUTS dataset. Each column shows the effect of removing one individual loss term. The full model trained with all loss components (H) produces sharp, well-aligned, and semantically coherent saliency maps, underscoring the complementary strengths of each loss term in optimizing both pixel-level accuracy and structural fidelity.



Figure 7. Qualitative ablation study by removing individual loss functions using the DUTS dataset. A: Image, B: Ground-Truth, C: Without B-IOU loss, D: Without CE loss, E: Without Focal Tversky loss, F: Without IOU loss, G: Without Topological Saliency loss, H: Our loss.

5. Conclusions

We propose a novel salient object detection framework that fuses multi-scale context, advanced attention, and uncertainty modeling to improve accuracy and boundary precision. Our model combines Recursive Channel Spatial Attention, Adaptive Cross-Scale Context modules, and an Edge Extractor to capture rich context and fine details, while Monte Carlo Dropout provides reliable uncertainty estimation. Experiments show superior performance on standard benchmarks, and boundary-sensitive, topology-preserving losses further enhance the precision and consistency of saliency maps.

References

[1] Nabila Abraham and Naimul Mefraz Khan. A novel focal tversky loss function with improved attention u-net for lesion segmentation. In *2019 IEEE 16th international symposium on biomedical imaging (ISBI 2019)*, pages 683–687. IEEE, 2019. [12](#)

[2] Radhakrishna Achanta, Sheila Hemami, Francisco Estrada, and Sabine Süstrunk. Frequency-tuned salient region detection. In *IEEE Conference on Computer Vision and Pattern Recognition (CVPR)*, pages 1597–1604, 2009. [2](#)

[3] Charles Blundell, Julien Cornebise, Koray Kavukcuoglu, and Daan Wierstra. Weight uncertainty in neural network. In *International conference on machine learning*, pages 1613–1622. PMLR, 2015.

[4] Ming-Ming Cheng, Shang-Hua Gao, Ali Borji, Yong-Qiang Tan, Zheng Lin, and Meng Wang. A highly efficient model to study the semantics of salient object detection. *IEEE Transactions on Pattern Analysis and Machine Intelligence*, 44(11):8006–8021, 2021.

[5] Noel Codella, Veronica Rotemberg, Philipp Tschandl, M Emre Celebi, Stephen Dusza, David Gutman, Brian Helba, Harald Kittler, and Allan Halpern. Skin lesion analysis toward melanoma detection 2018: A challenge hosted by the international skin imaging collaboration (isic). *arXiv preprint arXiv:1902.03368*, 2019. [12](#)

[6] Deng-Ping Fan, Ming-Ming Cheng, Yun Liu, Tao Li, and Ali Borji. Structure-measure: A new way to evaluate foreground maps. In *IEEE International Conference on Computer Vision (ICCV)*, pages 4548–4557, 2017.

[7] Deng-Ping Fan, Ming-Ming Cheng, Jiang-Jiang Liu, Shang-Hua Gao, Qibin Hou, and Ali Borji. Salient objects in clutter: Bringing salient object detection to the foreground. In *Proceedings of the European conference on computer vision (ECCV)*, pages 186–202, 2018.

[8] Deng-Ping Fan, Ming-Ming Cheng, Yun Liu, Tao Li, and Ali Borji. Enhanced-alignment measure for binary foreground map evaluation. In *International Joint Conference on Artificial Intelligence (IJCAI)*, pages 698–704, 2018.

[9] Deng-Ping Fan, Yingjie Zhai, Ali Borji, Jufeng Yang, and Ling Shao. Bbs-net: Rgb-d salient object detection with a bifurcated backbone strategy network. In *European conference on computer vision*, pages 275–292. Springer, 2020.

[10] Deng-Ping Fan, Jing Zhang, Gang Xu, Ming-Ming Cheng, and Ling Shao. Salient objects in clutter. *IEEE transactions on pattern analysis and machine intelligence*, 45(2):2344–2366, 2022. [7](#)

[11] Yuming Fang, Haiyan Zhang, Jiebin Yan, Wenhui Jiang, and Yang Liu. Udnnet: Uncertainty-aware deep network for salient object detection. *Pattern recognition*, 134:109099, 2023. [2](#)

[12] Mengyang Feng, Huchuan Lu, and Errui Ding. Attentive feedback network for boundary-aware salient object detection. In *Proceedings of the IEEE/CVF conference on computer vision and pattern recognition*, pages 1623–1632, 2019.

[13] Yarin Gal and Zoubin Ghahramani. Dropout as a bayesian approximation: Representing model uncertainty in deep learning. In *International Conference on Machine Learning*, pages 1050–1059, 2016. [4](#)

[14] Shang-Hua Gao, Yong-Qiang Tan, Ming-Ming Cheng, Chengze Lu, Yunpeng Chen, and Shuicheng Yan. Highly efficient salient object detection with 100k parameters. In *European Conference on Computer Vision*, pages 702–721. Springer, 2020.

[15] Z GongyangLi, Zhen Bai, Weisi Lin, and Haibin Ling. Lightweight salient object detection in optical remote sensing images via feature correlation. *IEEE Trans. Geosci. Remote Sens*, 60:5617712, 2022. [7](#)

[16] Qibin Hou, Ming-Ming Cheng, Xiaowei Hu, Ali Borji, Zhuowen Tu, and Philip HS Torr. Deeply supervised salient object detection with short connections. In *Proceedings of the IEEE conference on computer vision and pattern recognition*, pages 3203–3212, 2017. [2](#)

[17] Debesh Jha, Pia H Smedsrød, Michael A Riegler, Pål Halvorsen, Thomas de Lange, Dag Johansen, and Håvard D Johansen. Kvasir-seg: A segmented polyp dataset. In *International Conference on Multimedia Modeling (MMM)*, pages 451–462. Springer, 2020.

[18] Alex Kendall and Yarin Gal. What uncertainties do we need in bayesian deep learning for computer vision? *Advances in neural information processing systems*, 30, 2017.

[19] Alex Kendall, Vijay Badrinarayanan, and Roberto Cipolla. Bayesian segnet: Model uncertainty in deep convolutional encoder-decoder architectures for scene understanding. In *BMVC*, 2015.

[20] Aixuan Li, Jing Zhang, Yunqiu Lv, Bowen Liu, Tong Zhang, and Yuchao Dai. Uncertainty-aware joint salient object and camouflaged object detection. In *Proceedings of the IEEE/CVF conference on computer vision and pattern recognition*, pages 10071–10081, 2021. [2](#)

[21] Guanbin Li and Yizhou Yu. Visual saliency based on multi-scale deep features. In *Proceedings of the IEEE Conference on Computer Vision and Pattern Recognition (CVPR)*, pages 5455–5463, 2015. [12](#)

[22] Gongyang Li, Zhi Liu, Dan Zeng, Weisi Lin, and Haibin Ling. Adjacent context coordination network for salient object detection in optical remote sensing images. *IEEE Transactions on Cybernetics*, 53(1):526–538, 2022. [2, 3, 7](#)

[23] Yin Li, Xiaodi Hou, Christof Koch, James M Rehg, and Alan Yuille. The secrets of salient object segmentation. In *IEEE Conference on Computer Vision and Pattern Recognition (CVPR)*, pages 280–287, 2014. [2](#)

[24] Jiang-Jiang Liu, Qibin Hou, Ming-Ming Cheng, Jiashi Feng, and Jianmin Jiang. A simple pooling-based design for real-time salient object detection. In *Proceedings of the IEEE/CVF conference on computer vision and pattern recognition*, pages 3917–3926, 2019. [2](#)

[25] Jiang-Jiang Liu, Qibin Hou, Zhi-Ang Liu, and Ming-Ming Cheng. Poolnet+: Exploring the potential of pooling for salient object detection. *IEEE Transactions on Pattern Analysis and Machine Intelligence*, 45(1):887–904, 2022.

[26] Mingcan Ma, Changqun Xia, Chenxi Xie, Xiaowu Chen, and Jia Li. Boosting broader receptive fields for salient object detection. *IEEE Transactions on Image Processing*, 32:1026–1038, 2023. [7](#)

[27] Sina Mohammadi, Mehrdad Noori, Ali Bahri, Sina Ghofrani Majelan, and Mohammad Havaei. Cagnet: Content-aware guidance for salient object detection. *Pattern Recognition*, 103:107303, 2020.

[28] Jalaj Mukhoti, Alexander Kirsch, Yarin Gal, Alex Kendall, Ross McAllister, and Yarin Gal. Evaluating bayesian deep learning methods for semantic segmentation. In *BMVC*, 2018.

[29] Youwei Pang, Xiaoqi Zhao, Lihe Zhang, and Huchuan Lu. Multi-scale interactive network for salient object detection. In *Proceedings of the IEEE/CVF conference on computer vision and pattern recognition*, pages 9413–9422, 2020. [2](#)

[30] Xuebin Qin, Zichen Zhang, Chenyang Huang, Chao Gao, Masood Dehghan, and Martin Jagersand. Basnet: Boundary-aware salient object detection. In *Proceedings of the IEEE/CVF conference on computer vision and pattern recognition*, pages 7479–7489, 2019.

[31] Xuebin Qin, Zichen Zhang, Chenyang Huang, Masood Dehghan, Osmar R Zaiane, and Martin Jagersand. U2-net: Going deeper with nested u-structure for salient object detection. *Pattern recognition*, 106:107404, 2020. [2](#) [7](#)

[32] Kunye Shen, Xiaofei Zhou, and Zhi Liu. Minet: Multiscale interactive network for real-time salient object detection of strip steel surface defects. *IEEE Transactions on Industrial Informatics*, 20(5):7842–7852, 2024. [7](#)

[33] Jinming Su, Jia Li, Yu Zhang, Changqun Xia, and Yonghong Tian. Selectivity or invariance: Boundary-aware salient object detection. In *Proceedings of the IEEE/CVF international conference on computer vision*, pages 3799–3808, 2019.

[34] Yujia Sun, Geng Chen, Tao Zhou, Yi Zhang, and Nian Liu. Context-aware cross-level fusion network for camouflaged object detection. *arXiv preprint arXiv:2105.12555*, 2021. [7](#)

[35] Lv Tang, Bo Li, Yijie Zhong, Shouhong Ding, and Mofei Song. Disentangled high quality salient object detection. In *Proceedings of the IEEE/CVF international conference on computer vision*, pages 3580–3590, 2021.

[36] Xinyu Tian, Jing Zhang, Mochu Xiang, and Yuchao Dai. Modeling the distributional uncertainty for salient object detection models. In *Proceedings of the IEEE/CVF conference on computer vision and pattern recognition*, pages 19660–19670, 2023. [2](#)

[37] Sara Vicente, Joao Carreira, and Lourdes Agapito. Large-scale training of shadow detectors with noisy annotations. In *European Conference on Computer Vision (ECCV)*, pages 816–832. Springer, 2016. [12](#)

[38] Qibin Wang, Li Zhang, Guodong Wang, and Huchuan Lu. Learning to detect salient objects with image-level supervision. In *Proceedings of the IEEE Conference on Computer Vision and Pattern Recognition (CVPR)*, pages 136–145, 2017. [12](#)

[39] Qilong Wang, Banggu Wu, Pengfei Zhu, Peihua Li, Wangmeng Zuo, and Qinghua Hu. Eca-net: Efficient channel attention for deep convolutional neural networks. In *Proceedings of the IEEE/CVF conference on computer vision and pattern recognition*, pages 11534–11542, 2020. [2](#)

[40] Wenguan Wang, Jianbing Shen, Ming-Ming Cheng, and Ling Shao. An iterative and cooperative top-down and bottom-up inference network for salient object detection. In *Proceedings of the IEEE/CVF conference on computer vision and pattern recognition*, pages 5968–5977, 2019.

[41] Wenguan Wang, Shuyang Zhao, Jianbing Shen, Steven CH Hoi, and Ali Borji. Salient object detection with pyramid attention and salient edges. In *Proceedings of the IEEE/CVF conference on computer vision and pattern recognition*, pages 1448–1457, 2019. [2](#)

[42] Xiang Wang, Huimin Ma, Xiaozhi Chen, and Shaodi You. Edge preserving and multi-scale contextual neural network for salient object detection. *IEEE Transactions on Image Processing*, 27(1):121–134, 2017.

[43] Xue Wang, Li Zhou, Hao Shi, Ling Shao, and Ling Huang. Pyramid feature attention network for saliency detection. In *CVPR*, pages 3085–3094, 2020. [2](#)

[44] Sanghyun Woo, Jongchan Park, Joon-Young Lee, and In So Kweon. Cbam: Convolutional block attention module. In *Proceedings of the European conference on computer vision (ECCV)*, pages 3–19, 2018. [2](#)

[45] Runmin Wu, Mengyang Feng, Wenlong Guan, Dong Wang, Huchuan Lu, and Errui Ding. A mutual learning method for salient object detection with intertwined multi-supervision. In *Proceedings of the IEEE/CVF conference on computer vision and pattern recognition*, pages 8150–8159, 2019.

[46] Zhe Wu, Li Su, and Qingming Huang. Cascaded partial decoder for fast and accurate salient object detection. In *Proceedings of the IEEE/CVF conference on computer vision and pattern recognition*, pages 3907–3916, 2019. [2](#)

[47] Qiong Yan, Li Xu, Jianping Shi, and Jiaya Jia. Hierarchical saliency detection. In *Proceedings of the IEEE Conference on Computer Vision and Pattern Recognition (CVPR)*, pages 1155–1162, 2013. [12](#)

[48] Yi Zeng, Pingping Zhang, Jianming Zhang, Zhe Lin, and Huchuan Lu. Towards high-resolution salient object detection. In *Proceedings of the IEEE/CVF international conference on computer vision*, pages 7234–7243, 2019.

[49] Dingwen Zhang, Junwei Han, and Yu Zhang. Supervision by fusion: Towards unsupervised learning of deep salient object detector. In *Proceedings of the IEEE international conference on computer vision*, pages 4048–4056, 2017.

[50] Lu Zhang, Ju Dai, Huchuan Lu, You He, and Gang Wang. A bi-directional message passing model for salient object detection. In *Proceedings of the IEEE conference on computer vision and pattern recognition*, pages 1741–1750, 2018.

[51] Pingping Zhang, Dong Wang, Huchuan Lu, Hongyu Wang, and Xiang Ruan. Amulet: Aggregating multi-level convolutional features for salient object detection. In *Proceedings of the IEEE international conference on computer vision*, pages 202–211, 2017. [2](#)

[52] Qi Zhang, Linyuan Liu, Ruofei Han, Jianbing Shen, and Xiang Zhang. Progressive attention guided recurrent network for salient object detection. In *ICCV*, pages 5968–5977, 2019. [2](#)

[53] Xiaoning Zhang, Tiantian Wang, Jinqing Qi, Huchuan Lu, and Gang Wang. Progressive attention guided recurrent network for salient object detection. In *Proceedings of the IEEE conference on computer vision and pattern recognition*, pages 714–722, 2018.

- [54] Jia-Xing Zhao, Jiang-Jiang Liu, Deng-Ping Fan, Yang Cao, Jufeng Yang, and Ming-Ming Cheng. Egnet: Edge guidance network for salient object detection. In *Proceedings of the IEEE/CVF international conference on computer vision*, pages 8779–8788, 2019.
- [55] Xiaoqi Zhao, Youwei Pang, Lihe Zhang, Huchuan Lu, and Lei Zhang. Suppress and balance: A simple gated network for salient object detection. In *European conference on computer vision*, pages 35–51. Springer, 2020.
- [56] Xiaofei Zhou, Kunye Shen, and Zhi Liu. Admnet: Attention-guided densely multi-scale network for lightweight salient object detection. *IEEE Transactions on Multimedia*, 26:10828–10841, 2024. [2](#), [7](#)
- [57] Mingchen Zhuge, Deng-Ping Fan, Nian Liu, Dingwen Zhang, Dong Xu, and Ling Shao. Salient object detection via integrity learning. *IEEE Transactions on Pattern Analysis and Machine Intelligence*, 45(3):3738–3752, 2022.

6. Supplementary Material

We present additional details of our work in the following sections:

6.1. Network Architecture

6.1.1. Efficient Channel Attention (ECA) and Spatial Attention Mechanisms.

Efficient Channel Attention (ECA) focuses on capturing channel-wise dependencies without dimensionality reduction or excessive parameter overhead. Given an input feature map $x \in R^{B \times C \times H \times W}$, ECA applies global average pooling to squeeze the spatial dimensions:

$$z = \text{GAP}(x) \in R^{B \times C \times 1 \times 1}$$

The pooled vector is reshaped and permuted to $R^{B \times 1 \times C}$ to prepare for a 1D convolution along the channel dimension. This convolution with kernel size k models local cross-channel interactions efficiently:

$$z' = \sigma(\text{Conv1D}(z^\top)) \in R^{B \times C \times 1}$$

where σ denotes the sigmoid activation. After restoring the tensor shape to $R^{B \times C \times 1 \times 1}$, the attention weights modulate the original input feature map by element-wise multiplication, effectively re-weighting each channel.

Spatial Attention (SA) captures spatial importance by aggregating channel information through two pooling operations: max-pooling and average-pooling along the channel axis, producing two spatial descriptors:

$$M_{\text{max}} = \max_c(x), \quad M_{\text{avg}} = \text{mean}_c(x)$$

These descriptors are concatenated and passed through a convolutional layer with kernel size k followed by a sigmoid activation, generating a spatial attention mask:

$$M_s = \sigma(\text{Conv}_{k \times k}([M_{\text{max}}; M_{\text{avg}}]))$$

This mask is then applied to the input via element-wise multiplication, highlighting the spatially important regions.

Combined CBAM Block. The final CBAM block sequentially applies ECA and SA attention modules on the input feature map. Specifically, the input x is first channel-refined by ECA, then spatially refined by SA. A residual connection adds the original input to the output, preserving low-level features and stabilizing training:

$$\begin{aligned} x' &= x \times \text{ECA}(x) \\ x'' &= x' \times \text{SA}(x') \\ \text{Output} &= x'' + x \end{aligned}$$

6.1.2. Adaptive Cross-Scale Context Module (ACSCM).

Variant - ACSCM1: We adopt a simplified variant, ACSCM1, which omits the latter branch and uses *Recursive Channel-Spatial Attention (RCSA)* instead of CBAM for both current and previous stages.

We use the version of ACSCM with CBAM Attention for the first four ACSCM blocks and the version of ACSCM with RCSA Attention for the last ACSCM block.

6.2. Loss Function

1. Binary Cross-Entropy (BCE) Loss: BCE loss is a standard choice for binary segmentation tasks and is defined as:

$$\mathcal{L}_{\text{BCE}} = -\frac{1}{N} \sum_{i=1}^N [y_i \log(\sigma(p_i)) + (1 - y_i) \log(1 - \sigma(p_i))] \quad (25)$$

where p_i and y_i are the predicted logit and ground truth for pixel i , respectively. $\sigma(\cdot)$ denotes the sigmoid function and N denotes the number of pixels across all images in the batch. BCE ensures correct pixel-wise classification but lacks spatial awareness.

2. IoU Loss: Intersection-over-Union (IoU) loss is directly correlated with the performance metric and encourages better region-level prediction:

$$\mathcal{L}_{\text{IoU}} = 1 - \frac{\sum_i p_i y_i}{\sum_i p_i + y_i - p_i y_i + \epsilon} \quad (26)$$

The predicted probability for each pixel is denoted by p_i , where $p_i \in [0, 1]$, typically obtained by applying a sigmoid activation. The corresponding ground truth label is represented as y_i , where $y_i \in \{0, 1\}$. The term $\sum_i p_i y_i$ represents the intersection between the predicted and ground truth masks, summing over the element-wise product of predictions and labels. The union is given by $\sum_i p_i + y_i - p_i y_i$, accounting for all pixels where either the prediction or the ground truth is positive. To ensure numerical stability and prevent division by zero, a small constant ϵ is added to the denominator. The IOU loss complements BCE by enforcing alignment between predicted and ground truth regions, especially useful in cases of unbalanced foreground-background distributions.

3. Focal Tversky (FT) Loss: To further address foreground-background imbalance and emphasize hard-to-classify pixels (e.g., thin or ambiguous regions), we employ the Focal Tversky Loss [1]:

$$\mathcal{L}_{\text{FT}} = \left(1 - \frac{\text{TP}}{\text{TP} + \alpha \cdot \text{FP} + \beta \cdot \text{FN} + \epsilon} \right)^\gamma \quad (27)$$

where TP, FP, and FN represent the number of true positives, false positives, and false negatives, respectively, computed from the predicted probability map $P \in [0, 1]^{H \times W}$ and the ground truth binary mask $G \in \{0, 1\}^{H \times W}$. Specifically:

$$\text{TP} = \sum_{i,j} P_{i,j} \cdot G_{i,j} \quad (28)$$

$$\text{FP} = \sum_{i,j} P_{i,j} \cdot (1 - G_{i,j}) \quad (29)$$

$$\text{FN} = \sum_{i,j} (1 - P_{i,j}) \cdot G_{i,j} \quad (30)$$

Here, $P_{i,j}$ is the predicted foreground probability for pixel (i, j) , and $G_{i,j}$ is the corresponding ground truth label.

We set the weighting parameters to $\alpha = 0.7$, $\beta = 0.3$, and the focusing parameter to $\gamma = 0.75$, which biases the loss toward improving recall (by penalizing false negatives more heavily) while also reducing overconfidence in false positives. A small constant ϵ is added to the denominator to ensure numerical stability and avoid division by zero.

6.3. Dataset

The following datasets were used to test and compare the performance of our method:

1. DUTS:

The DUTS dataset [38] contains pixel-level saliency masks representing prominent objects in natural scenes. We use the 10,553 images (DUTS-TR) for training and 5,019 images (DUTS-TE) for testing.

2. ECSSD:

The Extended Complex Scene Saliency Dataset (ECSSD) [47] includes 1,000 images with semantically meaningful objects embedded in cluttered backgrounds. We use this dataset exclusively for testing.

3. HKU-IS:

HKU-IS [21] contains 4,447 images with multiple salient objects per image, often exhibiting low contrast with the background. This dataset is used only for testing.

4. SBU-Shadow:

The SBU Shadow Dataset [37] contains natural images with binary shadow masks. We use 4085 images for training and 638 images for testing.

5. ISIC2018 (Medical SOD):

The ISIC 2018 dataset [5] provides dermoscopic skin images with lesion-level annotations. 1886 images are used for training, and 808 images are used for testing.

6.4. Evaluation Metrics

Mean Absolute Error (MAE). MAE computes the average per-pixel absolute difference between the predicted saliency map \hat{Y} and the ground truth mask Y :

$$\text{MAE} = \frac{1}{H \times W} \sum_{i=1}^H \sum_{j=1}^W \left| \hat{Y}_{i,j} - Y_{i,j} \right|, \quad (31)$$

where H and W denote the height and width of the image, respectively. A lower MAE indicates higher prediction accuracy.

F-measure F_{\max} , F_{adaptive} , and F_{weighted} The F-measure combines precision and recall to evaluate the binary classification quality of the saliency map:

$$F_{\beta} = \frac{(1 + \beta^2) \cdot \text{Precision} \cdot \text{Recall}}{\beta^2 \cdot \text{Precision} + \text{Recall}}, \quad (32)$$

where β^2 is commonly set to 0.3 to weigh precision more heavily. We report:

- F_{\max} : the maximum F-measure over all thresholds.
- F_{adaptive} : F-measure computed at an adaptive threshold equal to twice the mean saliency value.
- F_{weighted} : a weighted version that considers the imbalance between foreground and background pixels.

Structure Measure (S_{α}). The Structure Measure evaluates structural similarity between prediction and ground truth by combining object-aware and region-aware structural comparisons:

$$S_{\alpha} = \alpha \cdot S_o + (1 - \alpha) \cdot S_r, \quad (33)$$

where S_o and S_r are object and region similarities, and α balances their contributions ($\alpha = 0.5$).

Enhanced-alignment Measure (E_{ϕ}). The Enhanced-alignment Measure evaluates the alignment of binary or continuous saliency maps with the ground truth:

$$E_{\phi} = \frac{1}{W \times H} \sum_{i=1}^W \sum_{j=1}^H \phi(\hat{Y}_{i,j}, Y_{i,j}), \quad (34)$$

where ϕ is a local alignment function capturing both global statistics and local pixel consistency.

Intersection over Union (IoU). IoU measures the overlap between the predicted binary mask P and the ground truth mask Y :

$$\text{IoU} = \frac{|P \cap Y|}{|P \cup Y|}. \quad (35)$$

A higher IoU indicates better segmentation overlap.

Computational Efficiency Metrics. In addition to accuracy and calibration metrics, it is essential to evaluate the computational complexity and inference efficiency of salient object detection models. These metrics determine the model’s suitability for real-time applications, deployment on edge devices, and large-scale processing.

- **Number of Parameters.** Denoted as `#Params`, this metric quantifies the total number of learnable weights in the model.
- **Floating Point Operations (FLOPs).** FLOPs measure the total number of multiply-add operations required to process a single image.
- **Inference Time.** Measured in milliseconds (ms), this metric reflects the average time required to forward-pass a single image through the model.
- **Frames Per Second (FPS).** FPS is the reciprocal of inference time and indicates the real-time processing capability of the model.